

DISLOCATION DENSITY CRYSTAL PLASTICITY BASED FINITE ELEMENT MODELING OF ULTRASONIC CONSOLIDATION

D. Pal*, B. E. Stucker⁺

*Department of Mechanical & Aerospace Engineering, Utah State University, Logan, UT 84322

⁺Department of Industrial Engineering, University of Louisville, Louisville, KY 40292

REVIEWED, August 17 2011

Abstract

A dislocation density based constitutive model has been developed and implemented into a crystal plasticity quasi-static finite element framework. This approach captures the statistical evolution of dislocation structures and grain fragmentation at the bonding interface when sufficient and necessary boundary conditions pertaining to the Ultrasonic Consolidation (UC) process are prescribed.

The hardening is incorporated using statistically stored and geometrically necessary dislocation densities (SSDs and GNDs) which are dislocation analogs of isotropic and kinematic hardening respectively. Since, the macroscopic boundary conditions during UC involves cyclic sinusoidal simple shear loading along with constant normal pressure, the cross slip mechanism has been included in the evolution equation for SSDs. The inclusion of cross slip promotes slip irreversibility, dislocation storage and, hence, cyclic hardening during the UC. The GND considers strain-gradient and thus renders the model size-dependent. The model is calibrated using experimental data from published refereed literature for simple shear deformation of single crystalline pure aluminum alloy and uniaxial tension of polycrystalline Aluminum 3003-H18 alloy. The model also considers the tension-compression asymmetry in case the model is applied for deformation processes in hexagonal close packed pure Titanium and its alloy counterparts which will be investigated further in our proposed research program. One of the significant macroscopic contributions from this model development is to successfully accommodate the elasto-plastic contact problem involved in UC.

The model also incorporates various local and global effects such as friction, thermal softening, acoustic softening, surface texture of the sonotrode and initial mating surfaces and presence of oxide-scale at the mating surfaces which further contribute significantly specifically to the grain substructure evolution at the interface and to the anisotropic bulk deformation away from the interface during UC in general. The model results have been predicted for Al-3003 H-18 alloy undergoing UC. A good agreement between the experimental and simulated results has been observed for the evolution of linear weld density and anisotropic global strengths macroscopically. Similarly, microscopic observations such as embrittlement due to grain substructure evolution and broken oxide layer at the UC interface has been also demonstrated by the simulation.

Introduction

As a direct result of ongoing research efforts in ultrasonic consolidation (UC) worldwide, it has become apparent that a new approach to modeling of UC bonding is needed. A model which provides a better understanding of the effects of process parameter changes on grain refinement,

plastic deformation and bonding during UC will better enable researchers to predict which materials will bond, how the mechanical properties of UC-produced parts can be improved, and how to better design the next generation of UC equipment.

The continuum properties of parts made using UC are strongly dependent upon the micromechanics of the bonded interface [1]. Interfacial-scale microstructures can be studied fundamentally using electron microscopy and can be used to correlate atomic and mesoscopic mechanisms of deformation to their continuum counterparts. A dislocation density-based crystal plasticity finite element model (DDCP-FEM) can capture the statistical distribution of dislocations, partials and various deformation mechanisms at the bonding interface as inputs to predict macroscopic deformation and mechanical property profiles as a function of energy input characteristics. These input characteristics are a function of the process parameters used in a UC machine, namely vibration amplitude, normal force, ultrasonic frequency, welding speed, sonotrode geometry and temperature.

Problem Formulation

It has been shown that material sheets subjected to UC undergo inhomogeneous plastic deformation through their thickness [1]. Classical continuum plasticity theories do not fully explain this phenomenon [2]. Therefore, a study of strain localization and grain refinement at the material interfaces during UC bonding is required. The following steps lead to the calculation of these localized strains and their effects.

1 Large Deformation Quasi-static formulation

The deformation map in space and time is described by the total deformation gradient tensor F (Figure 1). Applying the Kroner-Lee assumption, F is decomposed into elastic F_e and plastic gradient F_p tensors using multiplicative operator theory

$$F = F_e F_p \quad (\text{Eqn 1})$$

The plastic deformation gradient F_p includes constant volume plastic deformation without disturbance of the crystal lattice. Elastic distortion and rigid rotation of the lattice are described by a unique intermediate configuration free of local stresses.

2 The non-local dislocation density motivated material model

The flow response for dislocation density motivated crystal plasticity modeling in a given slip system ' α ' is given by (Ma 2006):

$$\dot{\gamma}^\alpha = \begin{cases} \gamma_0^\alpha \exp \left[\frac{-Q_{slip}}{K_B T} \left(1 - \frac{|\tau^\alpha| - \tau_{pass}^\alpha}{\tau_{cut}^\alpha} \right) \right] \text{sign}(\tau^\alpha) & \text{if } |\tau^\alpha| \geq \tau_{pass}^\alpha \\ 0 & \text{if } |\tau^\alpha| \leq \tau_{pass}^\alpha \end{cases} \quad (\text{Eqn 2})$$

where the pre-exponential variable $\dot{\gamma}_0^\alpha$ is the upper limit of the shear rate for the case where the Boltzmann factor is equal to 1, which can be found using:

$$\dot{\gamma}_0^\alpha = \frac{K_B T}{c_1 c_3 G b^2} \sqrt{\rho_P^\alpha} \quad (\text{Eqn 3})$$

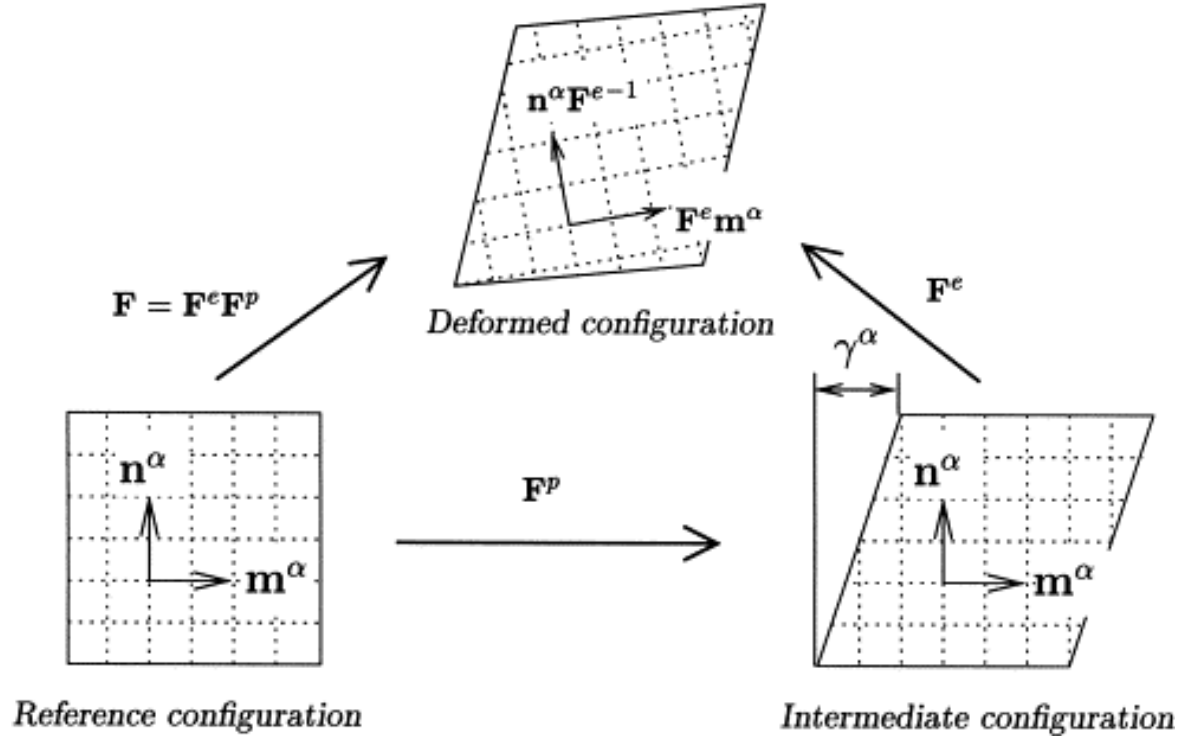


Figure1 Multiplicative decomposition of the total deformation gradient, $F=F^e F^p$. The rotation and stretching of the lattice are taken into account through the elastic deformation gradient F^e [3].

and the passing stress, τ_{pass}^α , caused by parallel dislocations can be found using:

$$\tau_{pass}^\alpha = c_1 G b \sqrt{\rho_P^\alpha} \quad (\text{Eqn 4})$$

and the cutting stress, τ_{cut}^α , at 0K caused by forest dislocations can be found using:

$$\tau_{cut}^\alpha = \frac{Q_{slip}}{c_2 c_3 b^2} \sqrt{\rho_F^\alpha} \quad (\text{Eqn5})$$

where Q_{slip} is the effective activation energy for dislocation slip.

The incompatibility in plastic deformation gradient and non-local geometrical non-linearity is introduced using ρ_{GND}^α which computes the geometrically necessary dislocations required to maintain continuity throughout the material. The evolution law for ρ_{GND}^α is:

$$\dot{\rho}_{GND}^\alpha = \frac{1}{b} \|\nabla_X \times (\dot{\gamma}^\alpha F_P^T) \tilde{n}^\alpha\| \quad (\text{Eqn6})$$

Material hardening at an integration point is both a function of ρ_{GND}^α and ρ_{SSD}^α (statistically stored dislocation density). The evolution laws for ρ_{SSD}^α are generally linear in shear rate (Eqn7).

$$\dot{\rho}_{SSD}^\alpha = c_4 \sqrt{\rho_F^\alpha} \dot{\gamma}^\alpha - c_5 \rho_{SSD}^\alpha \dot{\gamma}^\alpha + c_6 d_{dipole}^\alpha \rho_{mobile}^\alpha \dot{\gamma}^\alpha - c_7 \exp\left(-\frac{Q_{bulk}}{K_B T}\right) \frac{|\tau^\alpha|}{K_B T} (\rho_{SSD}^\alpha)^2 (\dot{\gamma}^\alpha)^{c_8} \quad (\text{Eqn7})$$

The various constants used in this modeling can be attributed to physical phenomena as shown in Table 1.

Material Parameter	Physical Meaning	Prescribed Value
Q _{slip}	Energy barrier for slip	3.0x10 ⁻¹⁹ J
Q _{bulk}	Energy barrier for climb (activated at higher temperatures)	2.4x10 ⁻¹⁹ J
c1	constant for passing stress (due to in-plane dislocations) (Equation 3)	0.1
c2	constant for jump width (Equation 4)	2.0
c3	constant for obstacle width (Equation 4)	1.0
c4	constant for lock forming rate (Equation 7)	1.5x10 ⁷ m ⁻¹
c5	constant for athermal annihilation rate (Equation 7)	10.0
c6	constant for dipole forming rate (Equation 7)	1.0x10 ⁻³⁰ m ⁻¹
c7	constant for thermal annihilation rate (Equation 7)	1x10 ⁷ m ⁵ c ⁸
c8	constant for non-linear climb of edge dislocation (Equation 7)	0.3
c9	constant for energy scaling at the interface	10 ⁻³

Table1 Physical Interpretation for various constants used in the Constitutive model

3 Global and Local Solution Strategies

The global and local solution strategy developed for solving the crystal plasticity constitutive model in section 2.2 is shown in Table 2.

Algorithmic Sequence (Implicit)
(A) Load steps $k=0,1,\dots,k_{\max}$
Set $v_0 = v_k, F_{p,0} = F_{p,k}, \rho_{SSD,0}^{\alpha} = \rho_{SSD,k}^{\alpha}, \rho_{GND,0}^{\alpha} = \rho_{GND,k}^{\alpha}$
(B) Iteration from $i=0,1,\dots, i_{\max}$
(I) Determine $r_i^{\alpha}, F_{p,k}^i$ and $\rho_{SSD,k}^{\alpha,i}$ with $\rho_{GND,k}^{\alpha,i} = \rho_{GND,k}^{\alpha}$ via local iteration at integration points (B-Bar Integration scheme)
(II) Determine $Q(u_k^i, \lambda_k^i), K_T(u_k^i)$ and solve $K_T(u_k^i)\Delta u = -Q(u_k^i, \lambda_k^i)$
(III) Displacement Increment: $u_k^{i+1} = u_0 + \Delta u_k^{i+1}$
(IV) Determine curl on all nodes calculate $\rho_{GND,k}^{\alpha,i+1} = \rho_{GND,0}^{\alpha} + \Delta \rho_{GND,k}^{\alpha,i+1}$ on all integration points
(V) Check (B) Local convergence: GND, SSD, and shear strain rate on each slip system (A) Global convergence for $ Q(u_k^i, \lambda_k^i) $
(VI) If (V) is true then: $v_{k+1} = v_k^{i+1}, F_{p,k+1} = F_{p,k}^{i+1}, \rho_{SSD,k+1}^{\alpha} = \rho_{SSD,k}^{\alpha,i+1}, \rho_{GND,k+1}^{\alpha} = \rho_{GND,k}^{\alpha,i+1}$ else goto (I)

Table2 Solution strategy for solving the crystal plasticity constitutive model with Nonlinear FEM.

First, the applied loading is applied incrementally as load steps. At the beginning of each load step ($k+1$), various nodal and integration point variables such as displacement (u), plastic deformation gradient (F_p), SSD and GND are initialized to their converged counterparts obtained in the previous load step. After initialization, an iterative procedure is used to solve for the local integration point variables. In every iteration (i), a local integration is performed via the B-Bar scheme to compute the stress, plastic deformation gradient and the hardness due to immobilized dislocation content (SSD). The stress is then resolved on a slip system to obtain the resolved shear stress (RSS, τ^{α}) followed by plastic shear strain rate $\dot{\gamma}^{\alpha}$ which further leads to the calculation of the stiffness matrix (C) at the integration point followed by a nodal updated tangent modulus (K) as a function of displacement. The tangent modulus is a measure of local stress with respect to local strain. This tangent modulus in uniaxial tensile plasticity is lower than the Young's modulus (E) since the force required to glide dislocations is less than the force required for moving perfect atomic planes. After the calculation of nodal tangent modulus, the internal nodal force based on stresses at the integration point and the integration algorithm (B-Bar) is used to calculate the force residual (Q). Solving the matrix-inversion problem posed in B

(II) in table 2, an increment in the displacement (Δu) is obtained for the current iteration (i). The increment in displacement is added to the current displacement for updating its value for the next iteration ($i+1$), if required. The increment in GND is calculated at this stage. The procedure is illustrated in Figure 2. First, the plastic deformation gradient (F_p) is linearly extrapolated from local integration points to the corresponding nodes. Next, the nodal value of F_p is averaged out since the node under consideration is connected to other elements. The curl ($\nabla \times \dot{\gamma}^\alpha F_p^T m_0^\alpha$) is calculated and returned to the integration points from their corresponding nodes in step 3. The curl ($\nabla \times \dot{\gamma}^\alpha F_p^T m_0^\alpha$) at integration points is multiplied by appropriate material variables to obtain GND for screw and edge dislocations in their normal and tangential directions respectively. To ensure that the local integration point has converged, the increments in $\dot{\gamma}^\alpha$, SSD and GND are compared against their respective threshold upper bounds. This is followed by global convergence, where the absolute value of the force residual (Q) is compared against a global threshold. Once both the local and global convergences are ensured, various nodal and integration point variables are predicted for the next load step; and the same sequence described here is repeated for the next load step ($k+1$).

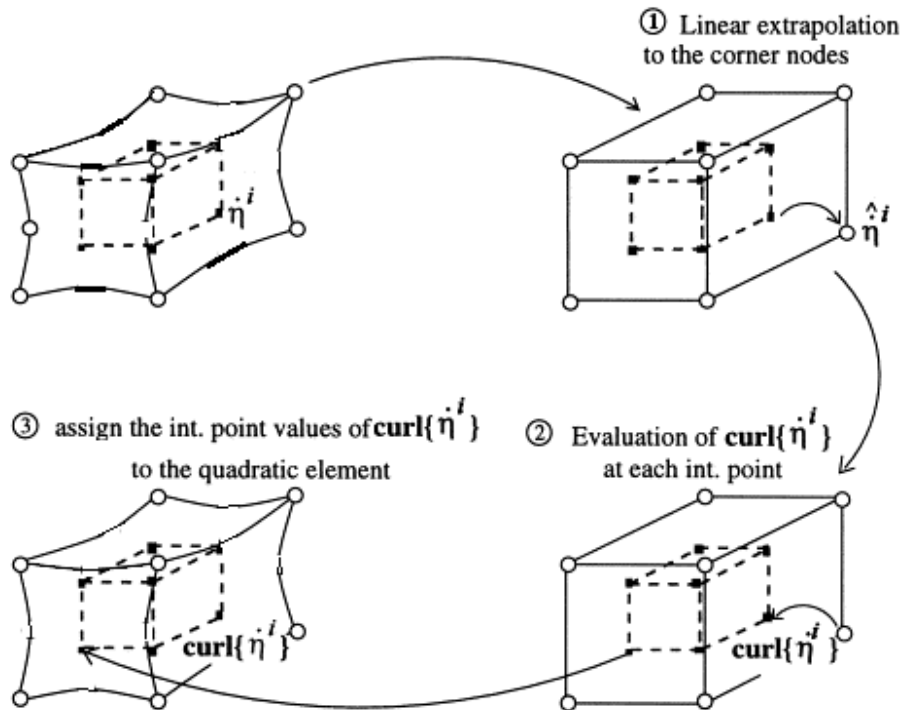


Figure2 Procedure to determine the slip-rate gradients within 3D trilinear elements with B-bar integration. The interpolation of the $\text{curl}\{\dot{\eta}_i\}$ is performed via an eight-noded solid element with $(2 \times 2 \times 2)$ integration.

4 Process Boundary Conditions

The model formulations and solution strategies in sections 2.1, 2.2 and 2.3 have been validated for simple boundary conditions such as simple shear and normal compressive loading [4]. The model results such as stress evolution, GND or inhomogeneous plastic deformation evolution and SSD or homogenous plastic deformation evolution are in good agreement with the experiments (Ma 2006) and (Siddiq 2007) respectively. UC process requires a simultaneous application of the abovementioned boundary conditions along with local interfacial contact based boundary conditions. Therefore based on the accuracy of the model established by validation of the results in the simple cases, more complex boundary conditions representing the UC process have been applied to the model and are discussed in this section. The model predictions for these complex boundary conditions and their comparison with the experiments will be discussed in section 3.

4.1 Global process boundary conditions

The schematic of the UC process in Figure 3 illustrates the global boundary conditions, namely normal compressive force, oscillation amplitude, weld speed and initial conditions like foil microstructures and surface roughness at the interface.

The schematic in Figure 3 has been converted into mathematical boundary conditions as shown in Figure 4.

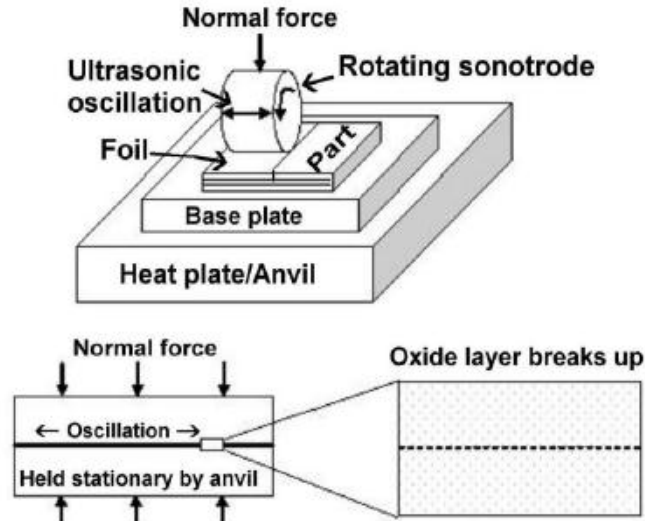


Figure3 Schematic of the UC process

The normal compression in UC is around 1200N -2000N for Aluminum alloy. The applied shear amplitude is of the order of $1\mu\text{m}$ - $25\mu\text{m}$ with foil thicknesses between $50\mu\text{m}$ - $200\mu\text{m}$ (a typically used foil thickness is $\sim 150\mu\text{m}$) and initial mating surface roughness varying from smooth ($R_a\sim 0.1\mu\text{m}$) to heavily surface damaged ($R_a\sim 5\mu\text{m}$). The mentioned surface conditions are only observed in the top part of the bottom foil because it has been freshly deformed by the sonotrode during deposition of the previous layer. The time period for one

oscillation is about 50 microseconds (corresponding to a sonotrode frequency of 20kHz). Since the travel speed of the sonotrode horn varies from 10-50 mm/s, the material point under UC loading experiences a maximum of 3000 material deformation cycles. Foils are typically composed of polycrystalline microstructures with random orientation as shown in [1]. The initial SSD has been assumed to be $5 \times 10^{13} \text{m}^{-2}$ [4]. The microscopic parameters required for simulations can be extracted from Table 1. Since, orientation imaging microscopy (OIM) data for the foils were not available, a random cubic polycrystalline microstructure has been assumed. The bottom foil and the top foil are comprised of 12 randomly generated crystals each, with the top foil having the same granular microstructure as the bottom foil.

4.2 Interfacial contact boundary conditions

For interfacial contact with friction, the contact boundary conditions can be formulated as follows:

$$(w^- - w^+) \cdot n \geq 0 \quad (\text{Eqn 8})$$

where w^- and w^+ are displacements of the nodes on the top of the bottom and bottom of the top foils in the vicinity of the interface respectively. n denotes the normal vector perpendicular to the interface. The normal vector is in the y-direction for this case.

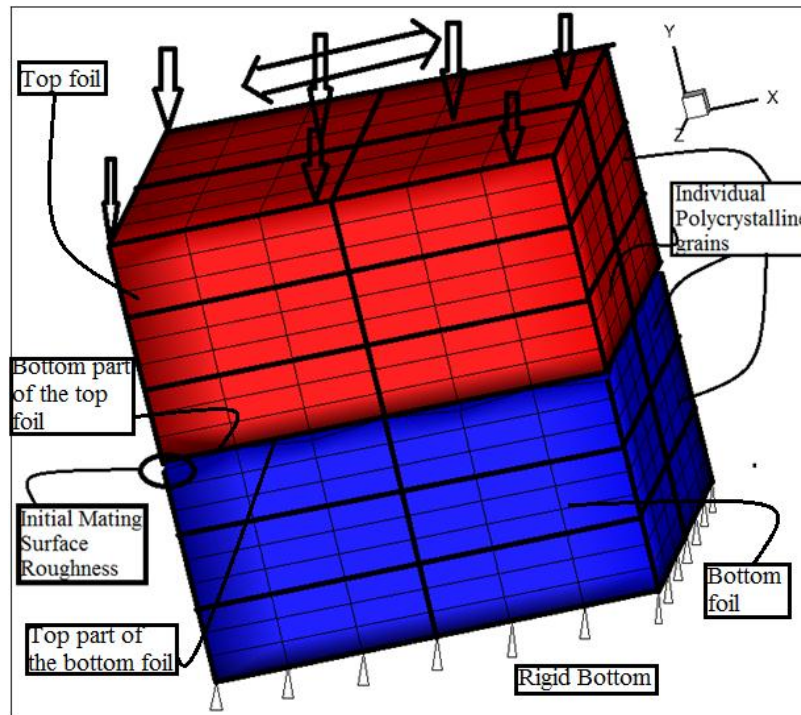


Figure4 Schematic showing Ultrasonic Consolidation global boundary conditions. The bottom of the model is held rigid. This assumption is only true for 2 foils on a large plate or a foil laid over a large plate.

In addition to equation 8, the normal traction components on the bottom of the top foil and top of the bottom foil should be compressive and tensile respectively. Also, from the point of view of force equilibrium, both of these traction components should be equal and opposite to each other as shown in equation 9.

$$t^+.n \leq 0, t^-.n \geq 0 \text{ and } t^+.n = -t^-.n \quad (\text{Eqn 9})$$

Equations 8 and 9 further lead to the Kuhn-Tucker conditions [11] for the normal traction and normal displacement components as demonstrated in equation (10)

$$(t^+.n)(w^- - w^+).n=0 \quad (\text{Eqn 10})$$

Further, similar to the normal traction components, the tangential components should be also in equilibrium (equation 11).

$$P_T t^+ + P_T t^- = 0 \quad (\text{Eqn 11})$$

where P_T is the tangential projection operator, given as:

$$P_T t = n \times (t \times n) \quad (\text{Eqn 12})$$

where \times denotes the cross product of two vectors.

For friction idealized by the Coulomb law, the maximum frictional force supported by the interface is:

$$g = \mu |t.n| \quad (\text{Eqn 13})$$

where μ is the coefficient of friction. The equations to be satisfied for the tangential component of interfacial tractions and displacements are as follows:

$$||P_T t|| \leq g \quad (\text{Eqn 14})$$

$$P_T w^- = P_T w^+ \quad \text{if } ||P_T t|| < g \quad (\text{Stick Condition}) \quad (\text{Eqn 15})$$

$$P_T (w^- - w^+) = -\lambda P_T t^+ \quad \text{if } ||P_T t|| = g \quad (\text{Slip Condition}) \quad (\text{Eqn 16})$$

Results and Discussion

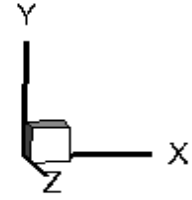
1 Effects of Friction at the UC interface

Two cases have been modeled to understand the effects of friction at the UC interface, one with a pure stick condition and the other with an appreciable amount of friction, replicating the friction behavior when the constituent foils are in contact with each other. The initial mating surface roughness has been fixed at an average roughness, $Ra \sim 5 \mu\text{m}$ with foil thickness being $150 \mu\text{m}$. The boundary conditions applied are (a) normal compression of 1800 N and (b) oscillatory shear amplitude of $16 \mu\text{m}$. The initial GND has been assumed to be 0 throughout the microstructure since the grain boundary area is negligible compared to the entire volume. The GND evolution in the bulk for one complete deformation cycle has been shown in Figure 5. Figure 5(a) illustrates the initial configuration for both the pure sticking and frictional sliding boundary conditions. During progressive loading in the pure sticking case, the mating interface experiences no resistance to the shear deformation. This leads to equal tangential displacements of the top and bottom foils in the vicinity of the interface. Therefore, the GND starts developing

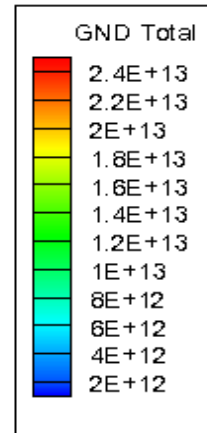
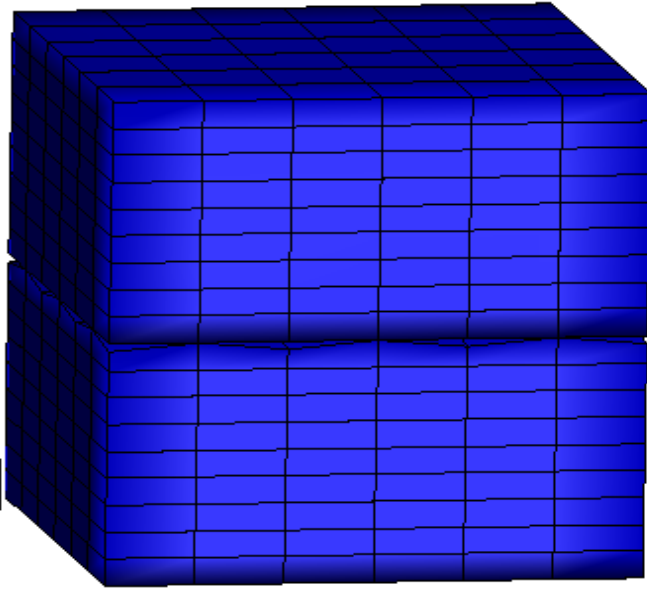
at the top surface of the top foil. On the contrary, in the frictional sliding case, the bottom foil in the vicinity of the interface experiences significant resistance due to friction. This further leads to much smaller tangential displacement of the bottom foil compared to the top foil in the vicinity of the interface. Henceforth, the GND is higher at the interface compared to the top surface of the top foil in this scenario. The GND evolution in both pure sticking and frictional sliding scenarios has been demonstrated in figures 5(b) through (e) corresponding to $(1/4)^{\text{th}}$, $(1/2)$, $(3/4)^{\text{th}}$ and 1 full deformation cycle during UC. It is also observed that the maximum GND after one complete cycle (figure 5(e)) in the frictional sliding case is greater than the pure sticking case by a factor of 2 suggesting more inhomogeneous deformation in the former. The motivation behind demonstrating these particular instants (figures 5(a)-(e)) comes from the fact that the applied shear loading either changes its direction or its sign at these instants. Also, the extent of GND evolution in the frictional sliding case limits itself to about 20 μm below the top surface of the bottom foil in the normal loading direction (y-axis). Therefore, this region experiences the maximum inhomogeneous plastic deformation, and kinematic hardening since the inhomogeneous plastic and kinematic hardening is directly proportional to the $\sqrt{\rho_{\text{GND}}}$ (Ma 2006). Moreover, continued GND evolution at the interface means a higher production of dislocations with either a positive or a negative sign. Therefore, a very high number of these GNDs lead to their annihilation and formation of new relaxed equiaxed subgrains. This phenomenon is termed dynamic recrystallization [6]. The emergence of recrystallized subgrains can be confirmed from experiments [1] where it has been observed that significant grain fragmentation has taken place near the interface on the top part of the bottom foil with a good amount of plastic flow beneath the region, as shown in figure 6.

This continued evolution of GND at the interface in the friction assisted case results in grain fragmentation (subgrain formation) by the end of 3000 material deformation cycles, since the average GND in the 20 μm strip below the top surface of the bottom foil reaches a value $\sim 6 \times 10^{15}$ dislocations/ m^2 in the top part of the bottom foil (Figure 7). The sub-grain diameter corresponding to this dislocation density is $\sim 2.28 \mu\text{m}$ [4].

(a)



(i) Pure Sticking



(ii) Friction

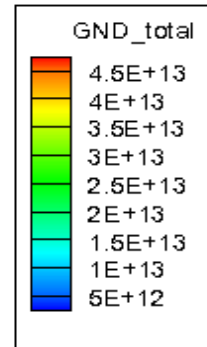
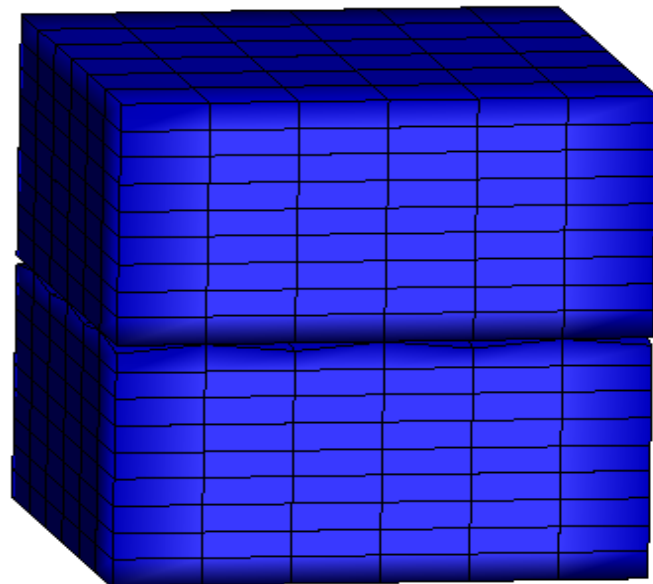


Figure 5(a) GND evolution at T=0 (i) Pure sticking (ii) Frictional sliding

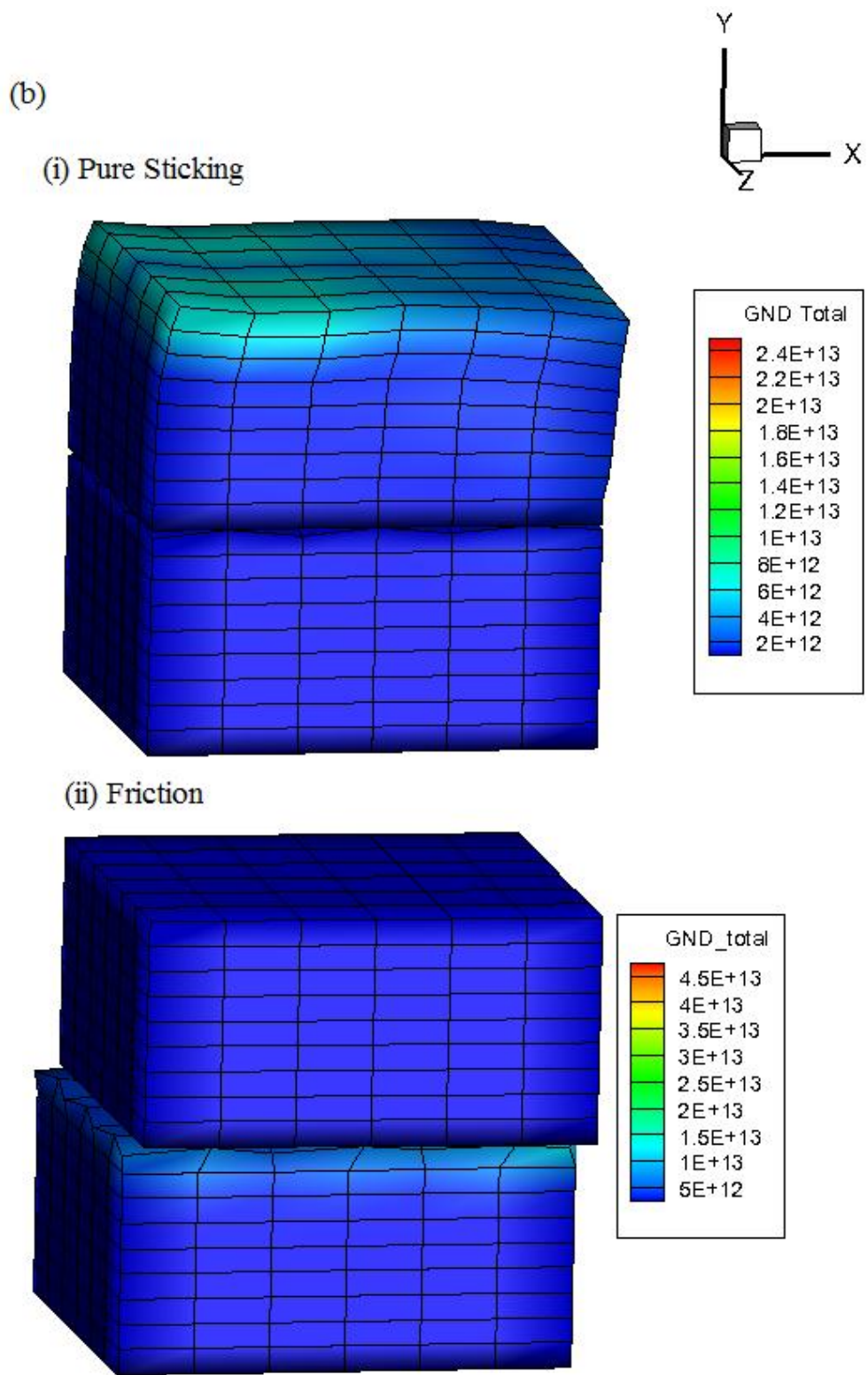
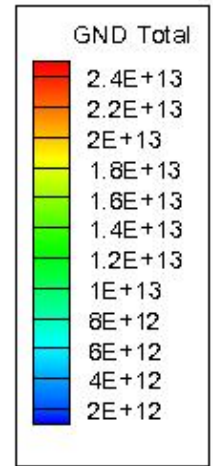
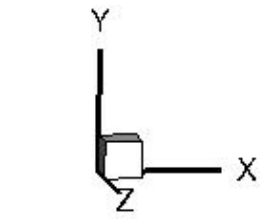
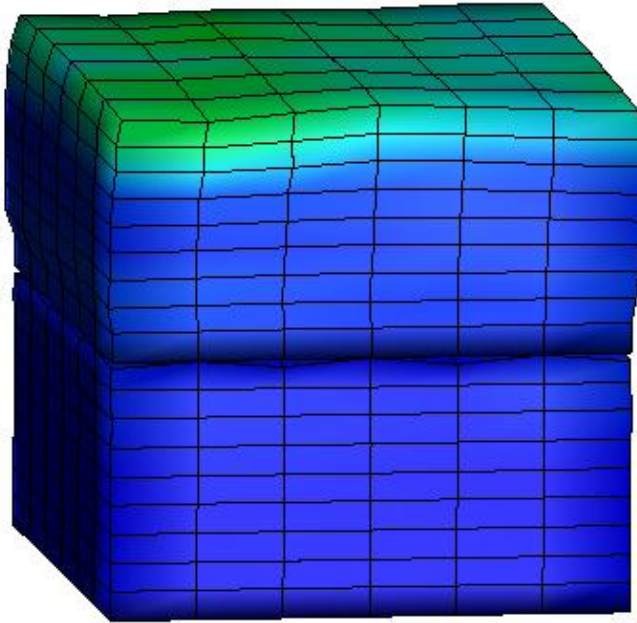


Figure 5(b) GND evolution at $T=1/4^{\text{th}}$ cycle (i) Pure sticking (ii) Frictional sliding

(c)

(i) Pure sticking



(ii) Friction

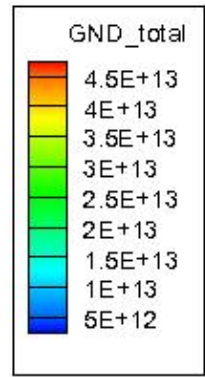
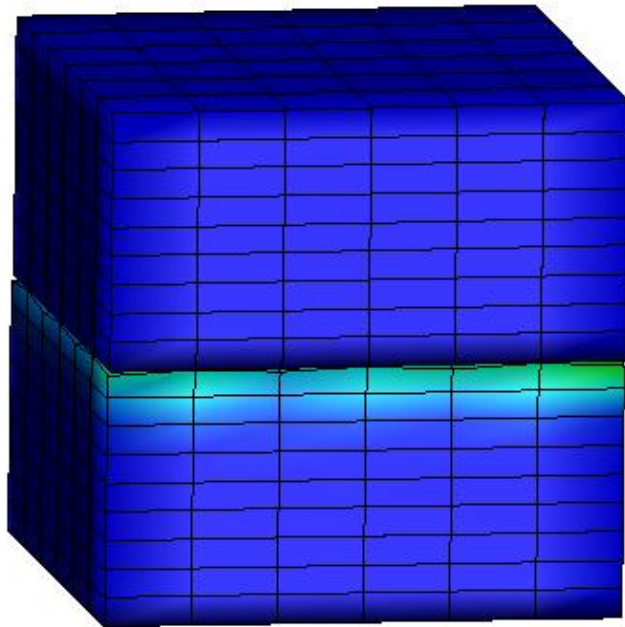
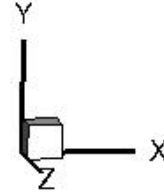
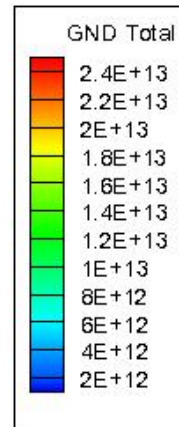
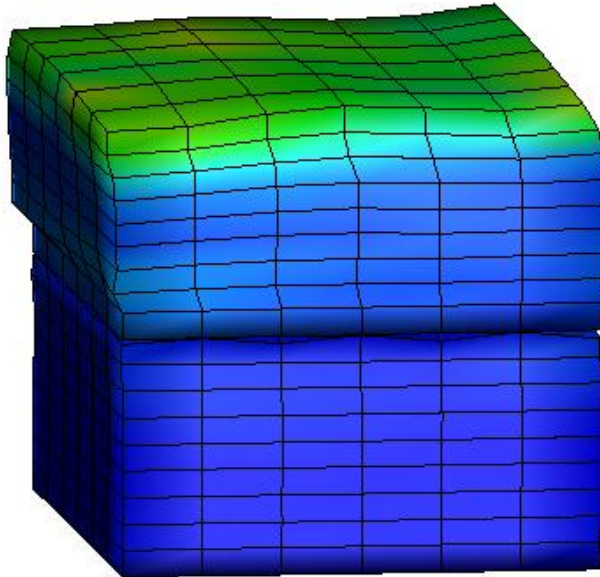


Figure 5(c) GND evolution at $T=1/2$ cycle (i) Pure sticking (ii) Frictional sliding

(d)



(i) Pure Sticking



(ii) Friction

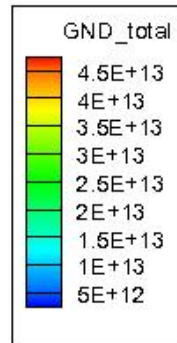
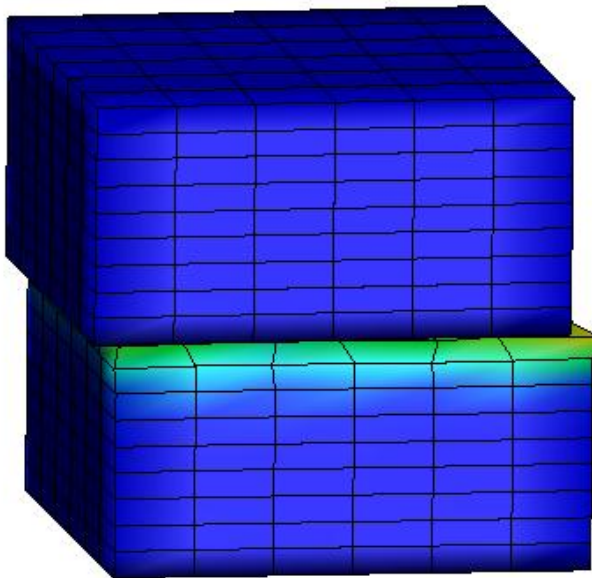
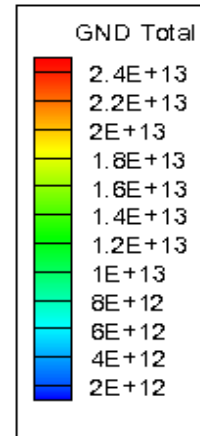
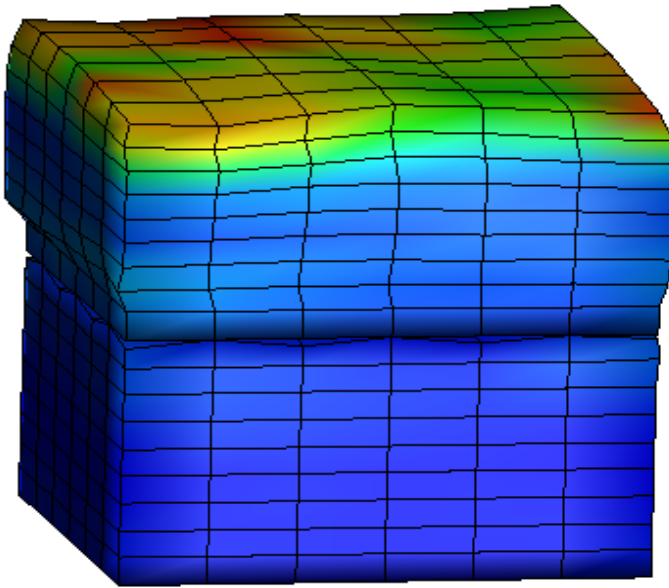
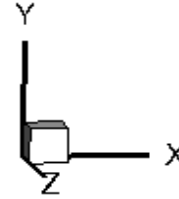


Figure 5(d) GND evolution at $T=3/4^{\text{th}}$ cycle (i) Pure sticking (ii) Frictional sliding

(e)

(i) Pure Sticking



(ii) Friction

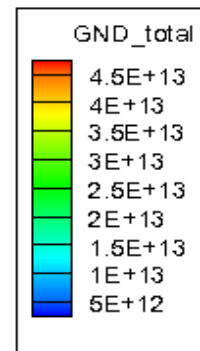
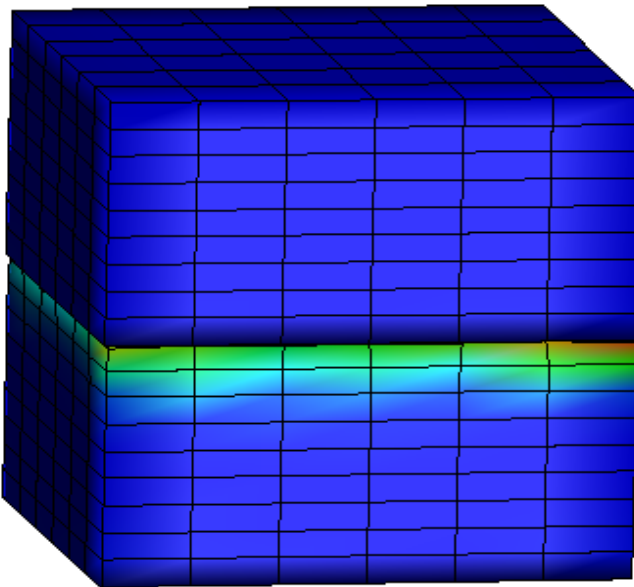


Figure 5(e) GND evolution at T=1 complete cycle (i) Pure sticking (ii) Frictional sliding

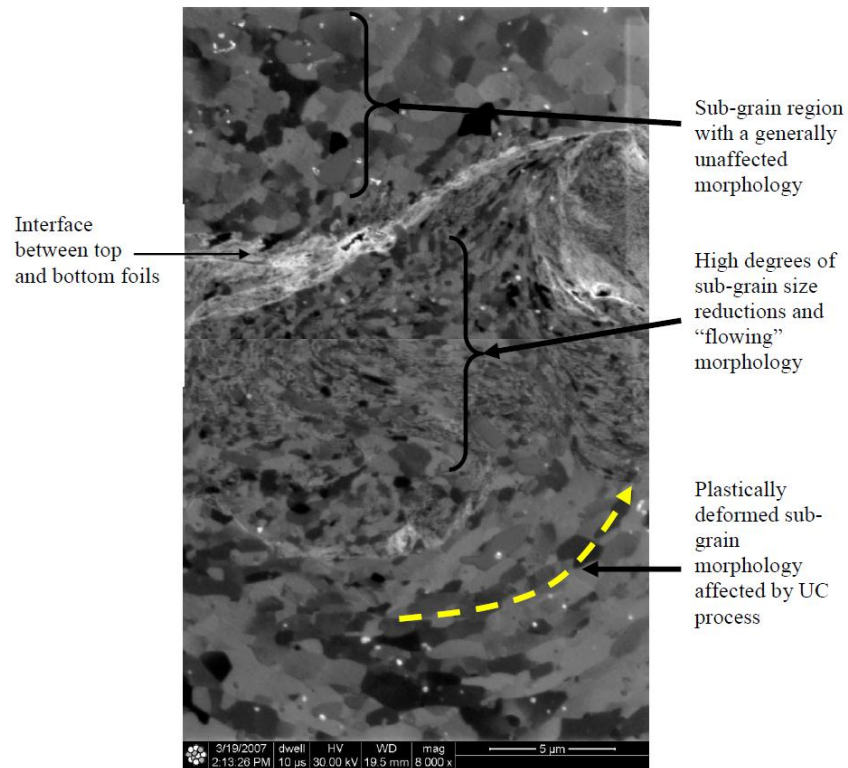


Figure6 Ion beam induced secondary electron micrograph of DBFIB-etch result for UC interface showing extent and depth of sub-grain size and morphology change as a result of the plastic deformation [1]

2 LWD evolution with cyclic deformation

Linear Weld Density measures the amount of bonded length to the total interfacial length, which is inversely proportional to the average gap between the mating surfaces at the UC interface. LWD generally increases with the amount of cyclic deformation. If the gap becomes zero, both the surfaces adhere and start plastically deforming together. Since the applied shear loading is cyclic during UC processing, the interface may lead to a fatigue type of failure and dynamic recrystallization at the interface when subjected to higher normal loads. Although the gap closure phenomenon has been included in the model, the prolonged fatigue phenomenon has not been included in the current set of simulations and is left for future work.

To quantify the effects of processing parameters such as oscillation amplitude and normal compressive load on LWD evolution, a design of experiments (DOE) approach was used by [5] to systematically evaluate the effects of process parameters and to identify the optimum parameter combination. Specific levels for each of the parameters were selected based on preliminary experiments, machine setting limits, and available published information. A Taguchi L16 orthogonal array was utilized in his study to determine the effects of individual process parameters. Table 4 lists the parameter combinations used for the experiments, and Figure 8 shows the experimental procedure.

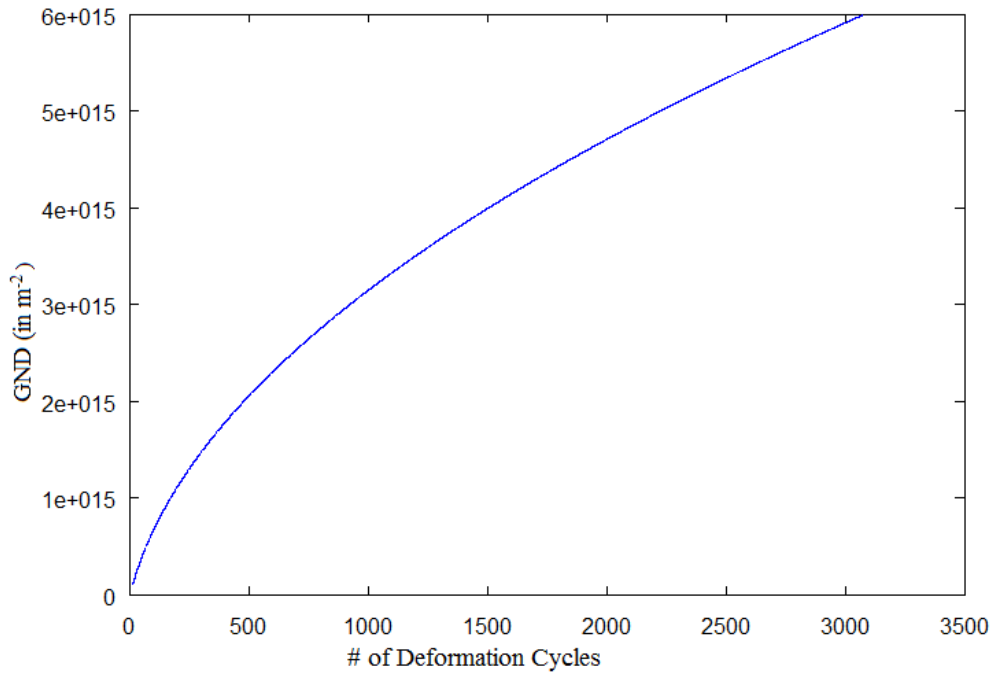


Figure7 GND evolution in the top part (~20 μm region) of the bottom foil for a Ra~5 μm in the top surface of the bottom foil.

Parameter	Level 1	Level 2	Level 3	Level 4
Oscillation Amplitude (μm)	10	13	16	19
Welding Speed (mm/s)	28	32	36	40
Normal Force (N)	1450	1600	1750	1900
Temperature (°F)	75	150	225	300

Table3 Parameters and levels selected for UC experiments [5]

Run#	Amplitude (μm)	Welding Speed (mm/s)	Normal Force (N)	Temperature (°F)
1	10	28	1450	75
2	16	40	1600	75
3	19	32	1750	75
4	13	36	1900	75
5	13	40	1750	150
6	19	28	1900	150
7	10	32	1600	150
8	16	36	1450	150
9	13	28	1600	225
10	10	36	1750	225
11	19	40	1450	225
12	16	32	1900	225
13	19	36	1600	300
14	16	28	1750	300
15	13	32	1450	300
16	10	40	1900	300

Table4 Taguchi L16 experimental matrix [5]

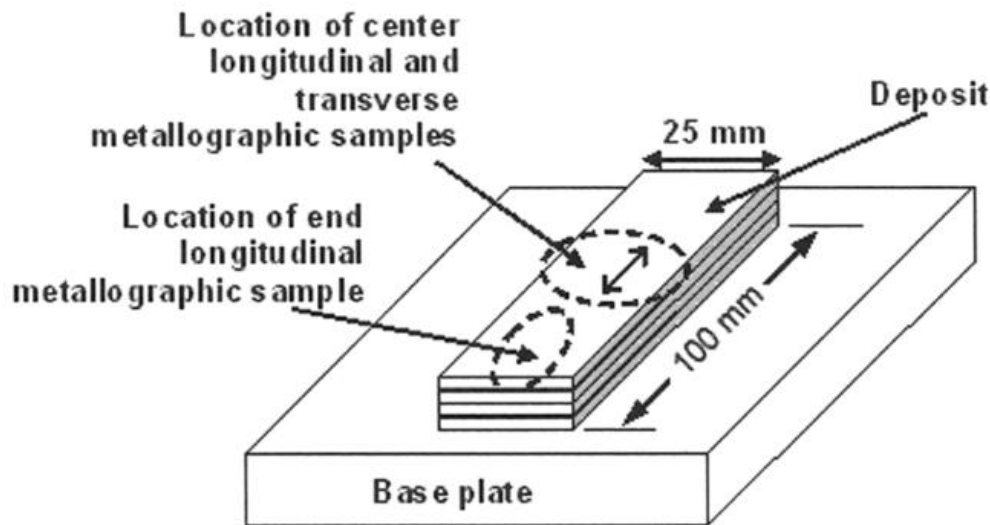


Figure 8 Schematic of Experimental UC Deposit Consisting of Four Layers. Welding occurred along the 100 mm direction. Metallographic sample locations are shown in the picture [5].

2.1 Effect of oscillation amplitude

The L16 Taguchi experiments conducted by [5] are an ideal DDCP-FEM model validation tool for UC. To investigate the effect of oscillation amplitude on LWD, four distinct simulations have been carried out with an applied normal load of 1750N for 3000 deformation cycles and applied ultrasonic amplitudes of 10, 13, 16 and 19 μm . The foil thickness was assumed to be 150 μm , with an average roughness of $R_a \sim 5 \mu\text{m}$ for the top part of the bottom foil. Figure 9 shows the average gap evolution between the mating surfaces as a function of increasing amount of cyclic deformation. It can be seen that for most amplitudes, the average gap no longer decreases after approximately the 10th cycle. For smaller amplitudes, the average gap decreases with increasing amplitude up to 16 μm . Above 16 μm the gap increases with increasing amplitude.

LWD has not been explicitly predicted in the simulation since the model treats gaps between the top and the bottom foils as 2 dimensional quantities whereas LWD is a one dimensional, linear quantity. However, the average gap can be used as an effective parameter for comparison with LWD, as LWD and average gap should show all of the same trends. A quantitative calibration between the average gap and LWD is left for future work.

As can be seen from figure 10, the average gap shows the same trends shown by [5], first increasing and then decreasing as a function of the applied ultrasonic amplitude. The optimum amplitude where the average gap is found to be the least was 16 μm for the applied boundary conditions. This is in good agreement with the experiments since the peak LWD has been observed at the same oscillation amplitude of 16 μm .

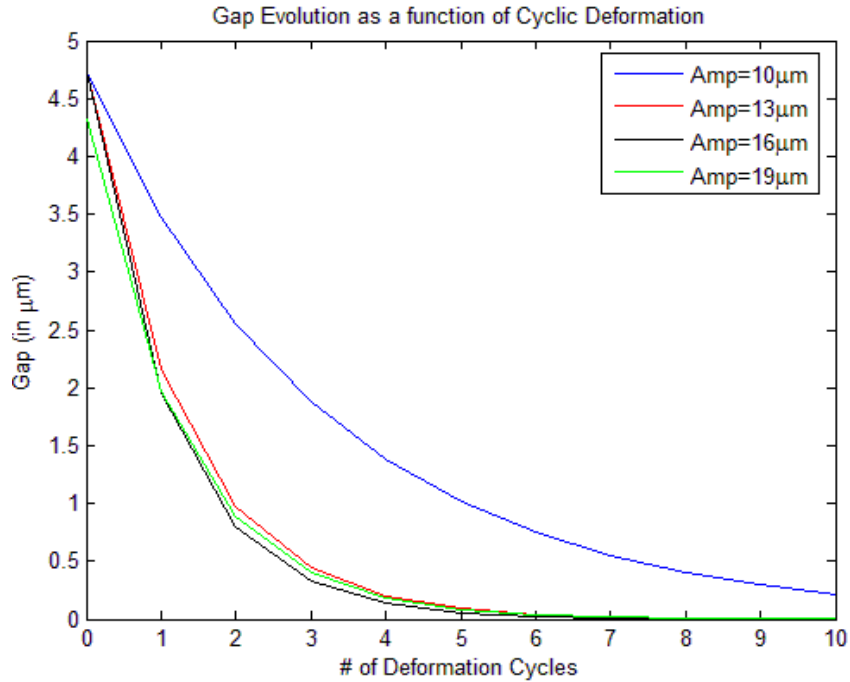


Figure9 Gap evolution (in μm) against number of deformation cycles with varying ultrasonic shear amplitudes.

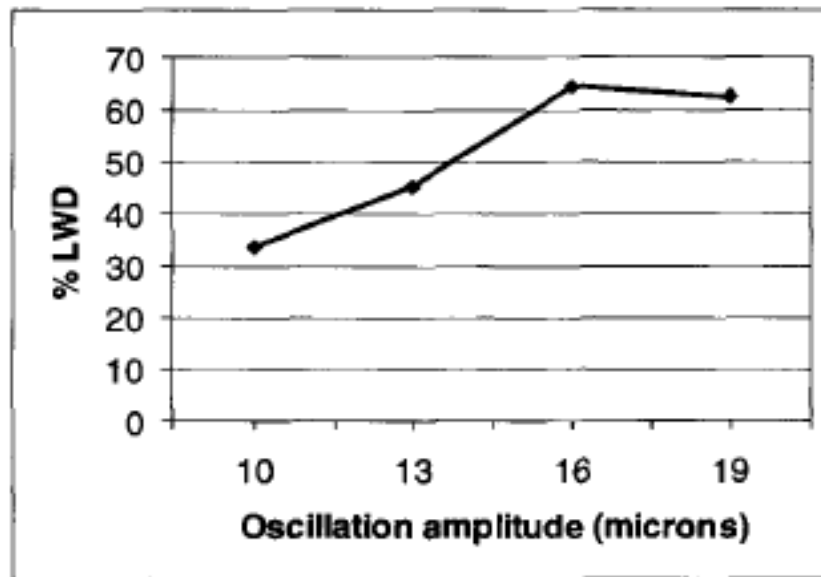


Figure 10: Effect of processing parameters on linear weld density, LWD vs. oscillation amplitude from [5]

2.2 Effect of Normal force

Similarly, to understand the effects of increasing normal load on gap closure/LWD, four applied normal loading scenarios have been considered. The applied normal loads were 1450, 1600, 1750 and 1900 N. The applied ultrasonic amplitude was 16 μm . The foil thickness and average roughness on the top part of the bottom foil were kept at 150 μm and $Ra \sim 5 \mu\text{m}$ respectively. Again, it can be seen (Figure 11) that there is no appreciable change/decrease in the average gap as a function of increasing cyclic deformation past the end of the 10th cycle for most cases.

It has been observed by Janaki Ram et al. [5] that when increasing the applied normal force, LWD increases up to a load of 1750 N. A further increase in normal load, however, lowered LWD. The most probable reason behind this LWD decrease is increase in the inhomogeneous plastic deformation with load near the top surface of the bottom foil. This leads to very high amounts of dynamic recrystallization which leads to dynamic failure of the bonded region at the interface. Therefore, in order to predict the experimental results, it will become necessary to incorporate fatigue crack nucleation and growth phenomena within the current DDCP-FEM.

The inclusion of fatigue phenomena is non-trivial for the following two reasons:

- The model assumes that once two nodes from the top and bottom surfaces are in contact with each other, the surfaces will be metallurgically bonded.
- A traction-separation law to mimic crack propagation with increasing cyclic deformation is not available from the literature.

In future work, a traction separation law will be formulated as a function of involved fatigue damage and further crack propagation to try to capture the bond degradation seen during experiments at higher loads.

In conclusion, the effects of oscillation amplitude and normal force on LWD evolution have been correctly modeled in this section with the exception of decreasing LWD with increasing normal force beyond a certain magnitude. Though the simulation parameter (average gap) characterizing the bonded region has not been calibrated quantitatively with LWD, it provides a good heuristic for bond characterization since the interfacial void closure is a 2 dimensional area based phenomenon.

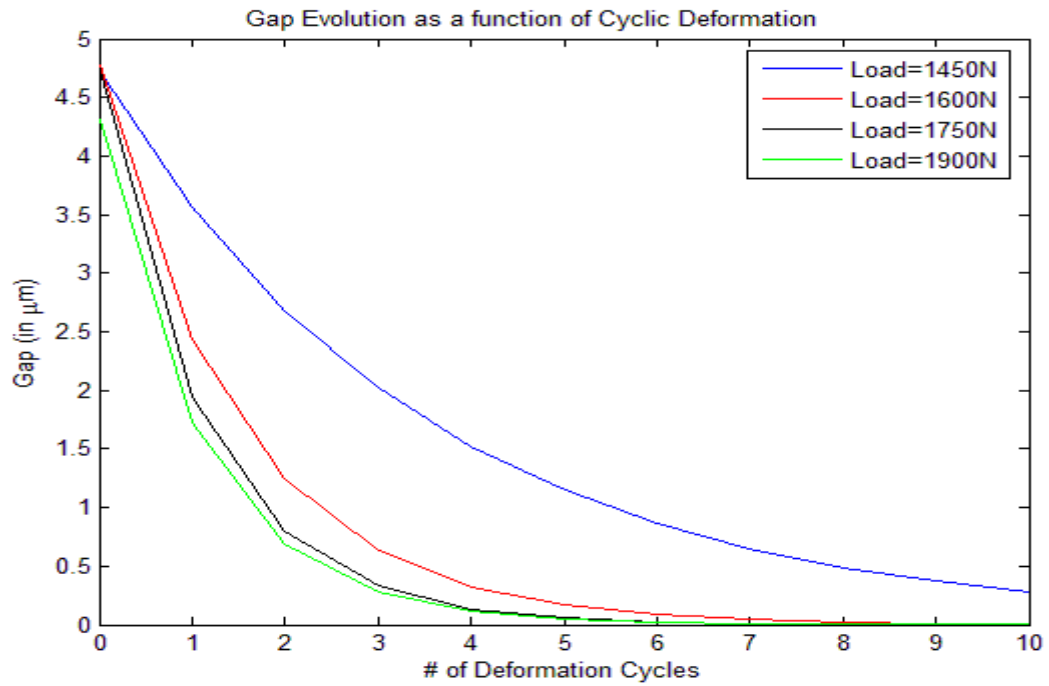


Figure11 Gap evolution (in μm) against the number of deformation cycles with varying normal loading scenarios.

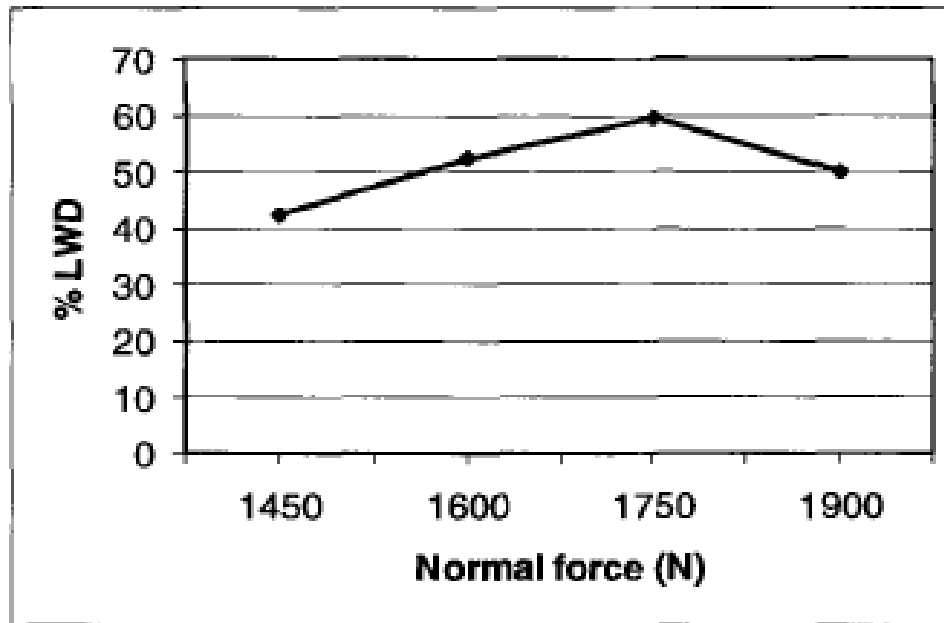


Figure12 Effect of processing parameters on linear weld density, LWD vs. Normal force from [5]

3 Effects of Mating Surface Roughness

The initial mating surface roughness at the top surface of the bottom foil is another important parameter for determining the amount and type of plastic deformation at the mating interface. The reason behind a rough top surface of the bottom foil during ultrasonic consolidation is because of the plastic work previously done by the sonotrode [8]. Two distinct simulations have been carried out to investigate the effects of surface roughness.

The simulation boundary conditions are: (a) normal compressive load of 1750N, (b) ultrasonic simple shear amplitude of 16 μm , (c) foil thickness of 150 μm , and (d) microstructure as shown in Figure 4. The top surface of the bottom foil has been assumed to have a roughness of $R_a \sim 0.1 \mu\text{m}$ in one case and $R_a \sim 5 \mu\text{m}$ in the second case. The lower roughness scenario represents two cases: (a) virgin foil depositing over a machined base plate, and (b) virgin foil deposition over a previously deposited and subsequently machined foil. It has been observed that the foil with lower surface roughness closes instantaneously in the first scenario whereas it takes around 10 deformation cycles to close the initial mating surface gap in the second scenario, as shown in figure 12. This further indicates a higher LWD in the low roughness case compared to the higher roughness case. This result is in good agreement with experiments [5], where the LWD is higher in between the machined base plate and virgin foil and lower in between the two layers comprising of sonotrode driven surface damaged foils. Similarly, GND evolution in the 20 μm strip below the interface sees a much higher rate of evolution in a higher roughness scenario than a lower roughness scenario as shown in figure 13, suggesting a greater amount of subgrain formation near the top surface of the bottom foil in the former case than in the latter case. This observation is in good agreement with experiments performed by [5] where it has been observed that the top surface of the bottom foil undergoes minimal subgrain formation since a smoother interface generally provides much less frictional resistance and in turn a lower value of the lattice curvature. The average subgrain diameter in the lower roughness scenario is $\sim 4.29 \mu\text{m}$ which is about 2X more compared to the higher roughness scenario $\sim 2.28 \mu\text{m}$, establishing a close match with the experimental observations [12].

Another important aspect is the mating interface shape, which has a higher rate of curvature in the higher roughness scenario than the lower roughness scenario, as shown in figure 14, after 3000 cycles. Again, this result can be validated using [5] depicting the interface shapes at the end of around 3000 cycles with lower and higher initial average roughness, $R_a \sim 0.1$ and $5 \mu\text{m}$ respectively. Clearly, the mating interface in the high surface roughness scenario shows a very high curvature and provides a good representation of the section at the interface demarcated in figure 13(a). Similarly, the planar interface in a low roughness scenario is a representative section of the interface demarcated in figure 13(b).

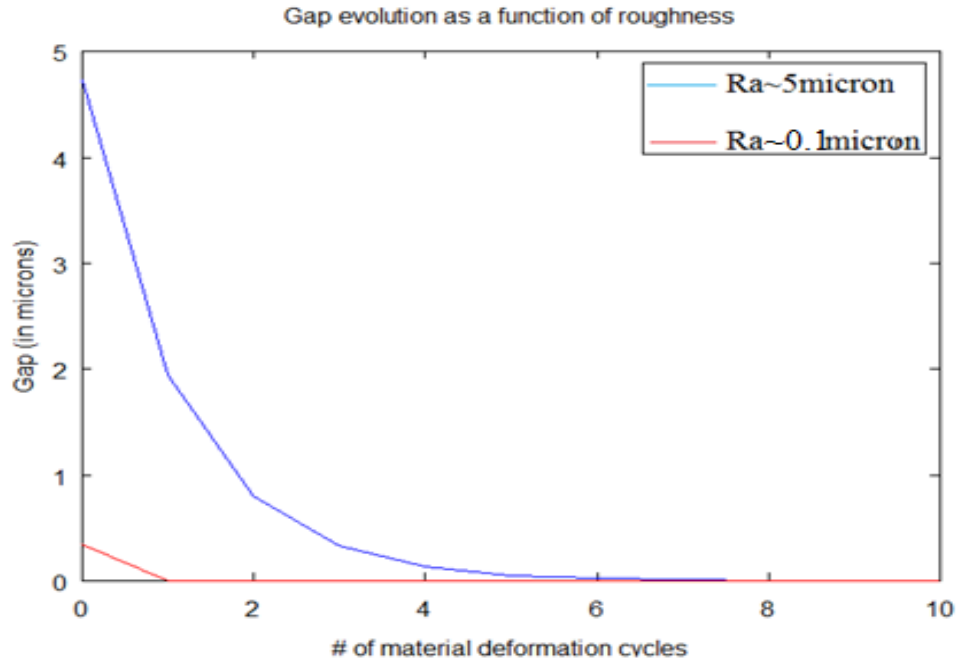


Figure 11: Gap evolution (in μm) against number of deformation cycles with varying bottom foil roughness

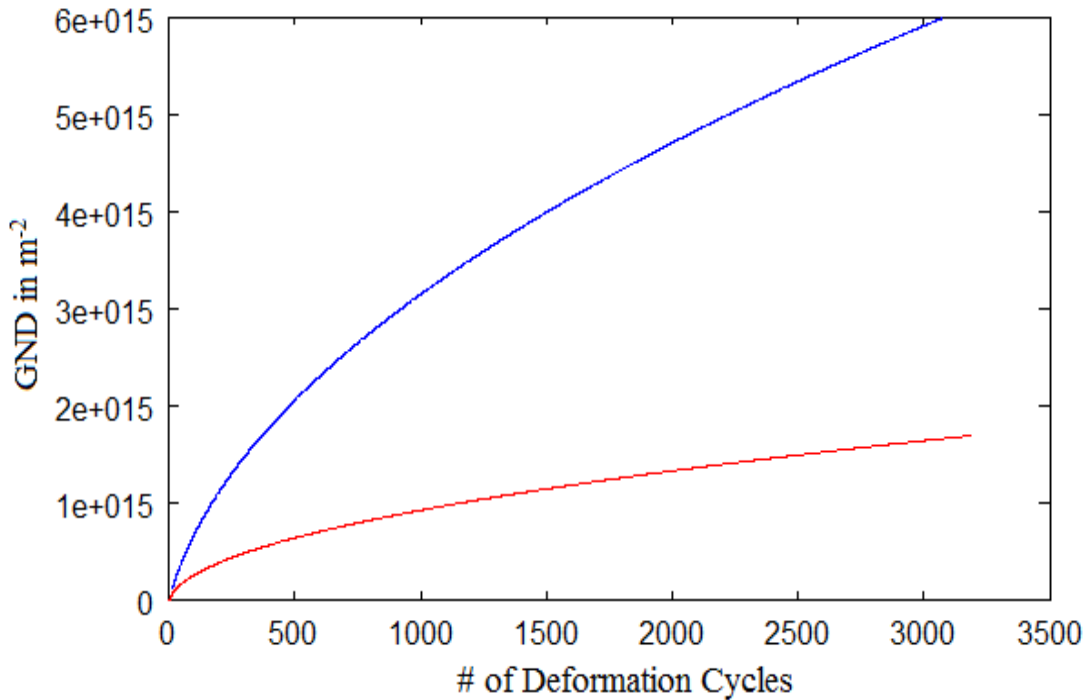


Figure12 GND evolution in the $20 \mu\text{m}$ strip below the interface against number of deformation cycles with varying bottom foil roughness. A higher GND at this location means more prominent subgrain formation. This result is in agreement with the experimental observations demonstrated in [5].

Interface shapes extracted from simulation after 3000 cycles

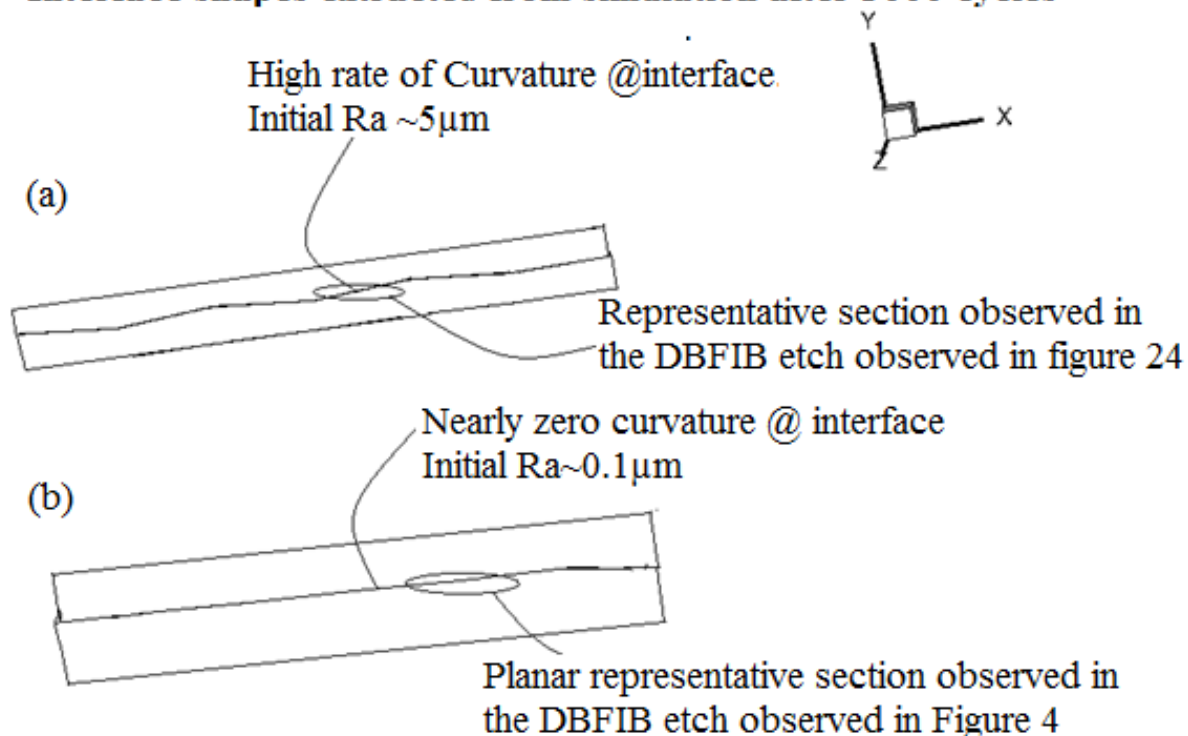


Figure13 Interface evolution against number of deformation cycles with varying bottom foil roughness.

4 Evidence of closure and relaxation at the interface

It has been observed that the gap between the top and the bottom foil being consolidated by UC undergoes closure and relaxation [7] based on its location at the interface and local stress state. Since, the gap between the top and bottom foil is prominent in the first few cycles, the closure-relaxation effect is also more pronounced in the earlier cycles.

The mechanism of gap closure and relaxation as a function of location and state of stress is summarized in figure 14. In the first quarter cycle at the rightmost locations, the top foil just above the interface undergoes a compressive state of stress and the bottom foil goes through a tensile state of stress. Also, at this point in time, the top foil at the leftmost locations just above the interface see a tensile state of stress and the bottom foil sees compressive stresses. Henceforth, the gap closes at an appreciable rate for the rightmost locations of the interface whereas it remains the same or slightly increases for the leftmost locations. In between the first quarter and half cycle, the top foil at the rightmost locations just above the interface develops a tensile state of stress whereas the bottom sees a compressive state of stress. Hence, the gap at these locations increase whereas the gap at the leftmost locations close because the top foil just above the interface develops a compressive state of stress and the bottom experiences tensile

stresses. The gaps at the leftmost locations continue to close because of the continued state of stresses in the top and bottom foils in the vicinity of the interface for the time between one half cycle and the last quarter of the complete cycle. Meanwhile at the rightmost locations, the top foil again starts seeing a compressive state of stress and the bottom foil experiences a tensile state of stress leading to gap closure. This state of stress continues for the rightmost locations in the last quarter of the complete cycle leading to further closure of the gap at these times. On the contrary, in the last quarter of the complete cycle, the leftmost locations again start seeing a tensile state of stress in the top foil and compressive stresses in the bottom foil leading to gap increase or gap relaxation.

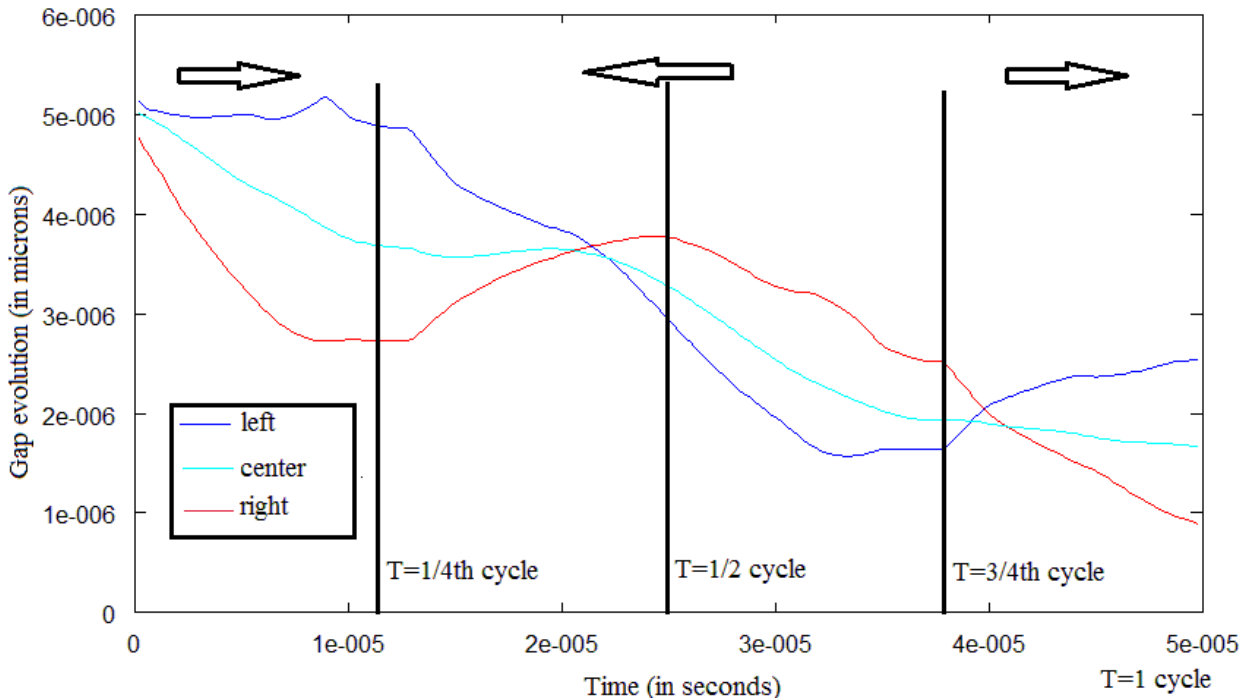


Figure14 The gap closure and relaxation as a function of location and applied loading at the mating interface. The arrows denote the direction of applied simple shear in a deformation cycle. The schematic represents the first cycle of UC deformation since the closure/relaxation mechanism is most pronounced in the transient stages.

It is essential to take gap closure and relaxation mechanisms into account while the UC machine is in operation since it aids in deciding the optimum amplitude required for proper deposition of virgin foils over previously deposited foils/machined substrate. If the sonotrode horn is operated at lower amplitudes than the transverse locations at which gap closure occurs, the interfacial contact rate is lower than the optimum leading to a lower rate of average gap minimization and lower LWD. Similarly for very high amplitudes, the transverse locations at which gap relaxation happens, the interfacial distance between the foils increase at a faster rate than the optimum, again leading to a lower rate of average rate of gap minimization and lower LWD. Henceforth, the optimum amplitude for average rate of gap minimization and LWD is achieved at an amplitude of 16 μm as above.

In future work, the weld speed will be explicitly applied as a boundary condition with applied normal compressive load and oscillation amplitude. It is anticipated that at the longitudinal locations ahead of the sonotrode, the top foil in the vicinity of the interface will experience a compressive state of stress whereas the bottom foil will experience a tensile state of stress causing the longitudinal interfacial gap to close. On the contrary, at the longitudinal locations behind the sonotrode, the top foil at the vicinity of the interface will experience a tensile state of stress whereas the bottom foil will experience a compressive state of stress causing the longitudinal gap to either remain closed (since the gap has already been closed due to transverse oscillatory motion of the sonotrode) or to rip open if a high enough weld speed is applied. Henceforth, a higher weld speed should decrease the LWD as the gaps behind the sonotrode starts to rip open. Another reason behind decreasing LWD with increasing welding speed is that the exposure time of the transverse weld cross-section to the sonotrode decreases with a higher welding speed, leading to incomplete bonding. The combined effect of gap closure and relaxation in the longitudinal direction along with incomplete bonding time on increasing welding speed has already been investigated and established by [5], and shown in figure 15. It is clear from figure 15 that the LWD decreases with increasing welding speed.

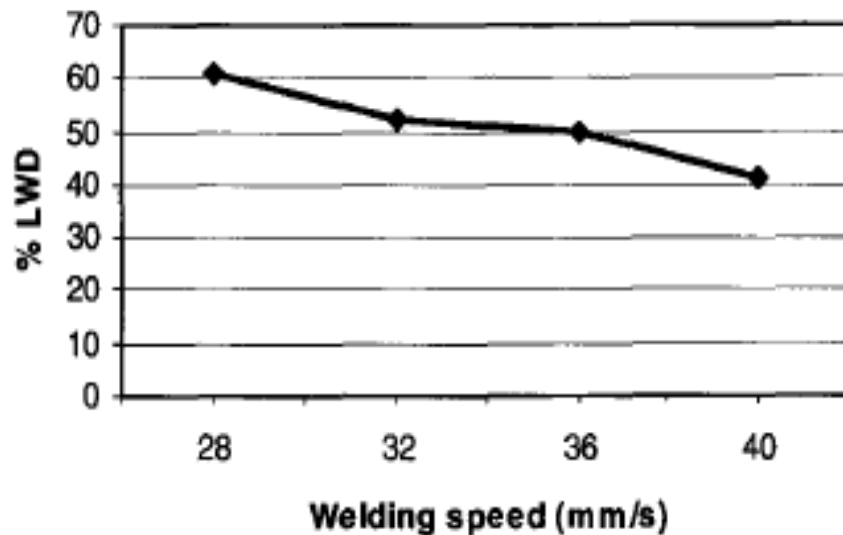


Figure15 Effect of processing parameters on linear weld density, LWD vs. weld speed from [5].

Conclusions and future work

1 Conclusions

A DDCP-FEM model has been formulated and tested based on UC boundary conditions comprised of simultaneous simple shear and normal compressive force applied to polycrystalline Al 3003 alloy at ultrasonic frequencies. The model was validated as follows:

- A higher normal force causes better bonding at the mating interface; though beyond a certain magnitude it results in a very high amount of in-homogeneous plastic deformation at the top surface of the bottom foil causing severe grain fragmentation and dynamic

fatigue failure. This is reflected in LWD evolution, where LWD first increases with increase in normal force and decrease beyond a certain magnitude [5].

- A higher amplitude enhances better bonding at the interface. Although beyond a certain magnitude, it enhances the rate of gap relaxation, which overcomes the rate of gap closure leading to lack of fusion at the interface. Gap closure and gap relaxation are directly and inversely proportional to LWD evolution respectively. Therefore, it has been predicted that the LWD would first increase with the oscillation amplitude and thereafter decrease beyond a certain magnitude. This prediction is consistent with experimental results [5].
- A higher welding speed is beneficial from the point of view of quick deposition of virgin foils on top of a previously deposited foil(s)/machined base plate. Although with increasing welding speed, the rate of gap relaxation at longitudinal locations behind the sonotrode becomes significant leading these closed gaps to rip open. Also, a higher welding speed leads to less exposure time of the transverse weld cross-section to the sonotrode. This combined effect further results in lack of fusion at the interface and a lower LWD as manifested in [5].

2 Future Work

The current model is able to predict the deformation response during UC processing but requires additional features to be realized as an efficient tool for material and parameter optimization in UC. The future accomplishments required in this paradigm are:

- To incorporate welding speed as a 3rd simultaneous applied load alongwith normal force and oscillation amplitude.
- To incorporate more number of foils being deposited on top of each other and their sequential consolidation. While doing this, the virgin foil for deposition will be assumed to have minimal initial GND and standard initial SSD content whereas for the previously deposited foils all the mesoscopic deformation variables such as SSD and GND will be stored from the previous deposition instant and applied as an initial condition for the fresh deposition.
- To formulate a traction-separation law which can quantify the delamination of foils as a function of applied normal and simple shear loading. This is important from the point of view of optimizing the weld speed required to avoid crack propagation due to fatigue after bond formation.
- To perform Orientation Imaging Microscopy (OIM) of the as-obtained and post-consolidated UC-foils to generate realistic microstructures required for realistic simulations.
- To formulate a homogenized model based on current DDCP-FEM to predict deformation during processing and in-service conditions. This is important since it will help with optimizing the initial orientation for the product build.
- To use the homogenized crystal plasticity model and non-destructive engineering metrics for closed-loop control (feed-forward and feed-back) of the UC machine.

In its current form, the model is still under development and has to be validated for other crystalline types such as single and polycrystalline variants of body centered cubic (BCC) materials such as Molybdenum and Tantalum, hexagonal close packed (HCP) materials such as Titanium and mixed alloys containing both HCP and BCC counterparts such as Ti6Al4V. These

alloys have been already demonstrated as potential materials for UC practice, though the biggest challenges to model these existing and new alloys which may serve as potential materials for UC are as follows:

- Determination of the active slip systems. For HCP and BCC, because of their limited slip system activity, the active slip systems are a function of the Schmid factor (projection of loading axis on the slip system) and temperature. Therefore, the active slip systems can either be obtained from experiments and theoretical explanations provided in the literature, phase field modeling or insitu TEM experiments in which the resolved shear strain evolution can be monitored.
- Incorporation of mesoscopic deformation mechanisms, for example Nickel based superalloys such as Inconel 718, which demonstrate significant twin activity [9] and BCC materials exhibiting Peierls resistance to mobile dislocation motion [10].
- Determination of mesoscopic material parameters (Q 's and c 's shown in Table 1).
- UC fabricated simple parts to validate model predictions.

REFERENCES

1. Johnson, K. 2008. Interlaminar subgrain refinement in ultrasonic consolidation. Wolfson School of Mechanical and Manufacturing Engineering, Loughborough University, UK.. PhD Thesis.
2. Bate, P. 1999. Modelling Deformation Microstructure with the Crystal Plasticity Finite-Element Method. *Philosophical Transactions: Mathematical, Physical and Engineering Sciences* 357: 1589-1601.
3. Ma, A. et al. 2006. A dislocation density based constitutive model for crystal plasticity FEM including geometrically necessary dislocations. *Acta Materialia*, 54: 2169-2179.
4. Pal, D. 2011. Dislocation density based finite element modeling of ultrasonic consolidation. Graduate School of Mechanical and Aerospace Engineering, Utah State University, USA. PhD Thesis.
5. Janaki Ram, G. D. et al. 2007. Effects of Process Parameters on Bond Formation During Ultrasonic Consolidation of Aluminum Alloy 3003. *Journal of Manufacturing Systems* 25: 221-238.
6. Rittell, D. and Osivski, S. 2010. Dynamic failure by adiabatic shear banding, *International Journal of Fracture* 162: 177-185.
7. Zhang, C.B. et al. 2006. A Study of Friction Behaviour in Ultrasonic Welding (Consolidation) of Aluminium. *Proceedings of the AWS Conference: Session 7: Friction and Resistance Welding/Materials Bonding Processes*
8. Friel, R.J. et al. 2010. The effect of interface topography for Ultrasonic Consolidation of aluminium. *Materials Science and Engineering A* 527: 4474-4483.
9. Uchic M.D. et al. 2006. Application of micro-sample testing to study fundamental aspects of plastic flow. *Scripta Materialia* 54:759-764.
10. Groger R., & Vitek V. 2009. Stress Dependence of the Peierls Barrier in BCC Metals. *Proceedings of the 5th conference of the Asian Consortium in Computational Materials Science, Hanoi, Vietnam.*

11. Dolbow, J. et al. 2001. An extended finite element method for modeling crack growth with frictional contact. *Computational methods in applied mechanics and engineering*, 190:6825-6846.
12. Sojiphan, K. et al. 2010. Stability of Microstructure in Al3003 Builds made by Very High Power Ultrasonic Additive Manufacturing. *Proceedings of the Solid Freeform Symposium, Austin, Texas*.